## Distribution Agreement

In presenting this thesis as a partial fulfillment of the requirements for a degree from Emory University, I hereby grant to Emory University and its agents the non-exclusive license to archive, make accessible, and display my thesis in whole or in part in all forms of media, now or hereafter now, including display on the World Wide Web. I understand that I may select some access restrictions as part of the online submission of this thesis. I retain all ownership rights to the copyright of the thesis. I also retain the right to use in future works (such as articles or books) all or part of this thesis.

Seung Kyu (Sam) Lee April 10, 2023

# Looking Past the Active Site: Equilibrium and Kinetic Studies of a Perturbed Second Coordination Sphere

by

Seung Kyu (Sam) Lee

Dr. Brian Dyer
Adviser

Chemistry

Dr. Brian Dyer

Adviser

Dr. Fang Liu

Committee Member

Dr. Craig Hill

Committee Member

Professor David Barba

Committee Member

2023

# Looking Past the Active Site: Equilibrium and Kinetic Studies of a Perturbed Second Coordination Sphere

By

Seung Kyu (Sam) Lee

Dr. Brian Dyer

Adviser

An abstract of
a thesis submitted to the Faculty of Emory College of Arts and Sciences
of Emory University in partial fulfillment
of the requirements of the degree of
Bachelor of Science with Honors

Chemistry

2023

Abstract

Looking Past the Active Site: Equilibrium and Kinetic Studies of a Perturbed Second Coordination Sphere

By Seung Kyu (Sam) Lee

As greenhouse gas emissions continue to increase at an alarming rate, researchers are scrambling to find an alternative fuel source to decrease the mass of greenhouse gases that are being emitted each day with our large dependence on fossil fuels. In the search for alternative, renewable, carbon-neutral sources of fuel, hydrogen gas has earned its spotlight due to its carbon-free combustion reaction, the product of which is only water. However, the problem with hydrogen lies in its production. In 2021, 84% of the 94 million tons of hydrogen gas was produced by steam methane reforming, a process that produces 5.5 tons of $CO_2$ for every ton of $H_2$. To free hydrogen of its carbon ties, many avenues are being explored, one of which is to turn to nature for its evolution-driven solution: hydrogenase. Hydrogenase is an enzyme that catalyzes the reversible oxidation of $H_2$, but many mechanistic and functional details of the second coordination sphere in hydrogenases are unknown. So, if the mechanistic and functional details of the protein scaffold can be fully characterized, it may be possible to develop novel and improved bio-inspired systems to produce carbon-neutral $H_2$. To this end, the aim of this thesis is to investigate the effect of E17D and E17Q point mutations in soluble hydrogenase I from *Pyrococcus furiosus* (*Pf* SH1) to gain insight into the effect of perturbing the second coordination sphere of *Pf* SH1 via Fourier-transform and transient absorbance infrared spectroscopy. In conjunction with previous studies, our results indicate that the glutamic acid of the second coordination sphere in *Pf* SH1 greatly affects the catalytic landscape of the enzyme beyond the proton transfer chain.

# Looking Past the Active Site: Equilibrium and Kinetic Studies of a Perturbed Second Coordination Sphere

By

Seung Kyu (Sam) Lee

Dr. Brian Dyer

Adviser

A thesis submitted to the Faculty of Emory College of Arts and Sciences
of Emory University in partial fulfillment
of the requirements of the degree of
Bachelor of Science with Honors

Chemistry

2023

Acknowledgements

I joined Dr. Dyer's laboratory at the tail end of the COVID pandemic the time in this lab has been nothing but delightful and inspiring. I would like to thank every lab member who nurtured a friendly and cooperative environment which made my past two years of research very enjoyable. Every question I may have had, every mistake and every learning moment were met with such great individuals who were more than willing to help and whose dispositions were genuine, great mentors. I have grown a lot as a researcher during my time in the Dyer lab, and I would like to thank every former and present lab member as well as the legendary Dr. Dyer for their support and assistance every step of the way. I would like to extend a special thank you to David White, Alexia Prokopik, Seth Wiley, Greg Vansuch, Caterina Netto, Tapas Haldar, and Dr. Dyer for their amazing leadership and extensive assistance in the lab and life in general. I would also extend a warm thank you to my peers—Kristina Trifonova, Ritika Pandey, and Sarah Bell—who have all made the undergraduate experience a delightful one.

I would also like to thank every one of my dear friends who I have made during my time here at Emory feel like a summer camp: Ruth Nelson, Joe Ambarian, Steve Gaunt, Edmund England, Schuyler Arn, Israel Negrete-Abreu, and so many more! All the nights spent together working on assignments, all the days spent goofing around, all the memories I will cherish forever—I thank you all for the invaluable memories and experiences we have created together.

Last but most certainly not least, I would like to extend a very big thank you to my family, as they cheer me on from Korea. To all of my grandparents, who are a part of my core childhood memory. To my dad, Jeong Jun Lee, who has spent over a decade apart from his family to support us from Korea: you are the greatest role model and dad one could ask for, and I am always impressed by your resilience and optimism that shines through the darkest nights. To my mom, Su Jung Park, who had so much on her plate raising a family in a foreign country, balancing school, work, motherly duties, and driving hours and hours to get her three children where they need to be at a moment's notice: you are also the greatest role model next to dad as well as the most amazing mom that one could ask for, and it will always impress me how you have endured so many hardships while raising a family in a foreign country with little to no support system. To my older brother, Dong Kyu Lee, who has guided my turbulent teenage years and shaped me to be a decent person: your kind heart and infectious optimism has made my days infinitely better. The days we would spend gaming together, the way you so dearly cherish your younger brother, and the many life lessons you have taught me have played a large part in my personal development, and I will cherish our memories forever. Last but not least, to my sister, Yea Sol Lee, who has been through so much yet still finds the energy to smile and share a moment of happiness with me, you are the best sister I could ever ask for. I still remember the days when you would pick me up from kindergarten with a warm fish-shaped bun that I had always sung about.

Table of Contents

List of Tables



List of Figures

# Chapter 1. Introduction and Motivation of Research

## *1.1. The climate crisis*

Although it may seem like a buzzword used by mass media to attract viewership, climate change is a real and imminent threat to humanity. According to the Intergovernmental Panel on Climate Change's (IPCC) 2022 report from its sixth assessment cycle, atmospheric greenhouse gas (GHG) content had reached a 1.5-fold net increase in 2019 since 1990.[1] As the solar radiation hits Earth, it absorbs the incoming radiation and re-radiates as infrared radiation. As it turns out, vibrational modes of GHGs absorb infrared radiation, which effectively traps infrared radiation—or heat—in the atmosphere. Dire consequences stemming from global surface temperature increases are bound to come as GHGs continue to be introduced to the atmosphere at an alarming rate.[2] Presently, the loss of glaciers and ice sheets, rise of sea levels, and extreme weather fluctuations have been attributed to the increase of GHGs in the atmosphere.[3] If GHGs continue to increase, more intense and longer occurrences of the aforementioned phenomena are inevitable.[3]

## *1.2. The hydrogen economy*

In the broader effort of reducing GHG emissions, the switch from fossil fuel to renewable energy sources is perhaps the most important. Of the various renewable energy sources, one promising source is hydrogen gas ($H_2$), recognized as an alternate fuel under the Energy Policy Act of 1992.[4] Recent developments in hydrogen applications include 1) hydrogen fuel-cell (HFC) electric vehicles, which are magnitudes more efficient than gasoline vehicles and preferable in energy-intensive applications and 2) HFC backup generators, which boast outstanding stability and have kept telecommunication towers online for more than 100

hours when hurricane Sandy devastated the east coast of the U.S.[4-6] Beyond energy generation, hydrogen plays a key role in chemical (feedstock for ammonia production), petrochemical (hydrocracking in gasoline production), and steelmaking sectors, which are the very backbones of agriculture, transportation, and general manufacturing, respectively.[5] However, despite promising evidence for $H_2$ as an alternate fuel source and its imperative role in many essential sectors and processes, meeting the hydrogen budget in an eco-friendly way proves to be a challenge.

Being composed of only two hydrogen atoms, molecular hydrogen can be produced from a variety of sources including natural gas, coal, biomass, and water.[4] However, of the 94 million tons of the global budget of $H_2$ in 2021, 77.1 million tons (82%) were produced by fossil-fuel-based methods such as steam methane reforming and coal gasification.[4,5,7] Whereas low-emission methods such as electrolysis accounted for only 8.46 million tons (9%) of the $H_2$ produced in 2021.[5] Steam methane reforming is a method in which high-temperature steam (around 1000 °C) is reacted with methane to form carbon monoxide and hydrogen gas ($CH_4 + H_2O + \text{heat} \rightarrow CO + 3H_2$), after which the carbon monoxide byproduct is further reacted in the water-gas shift reaction ($CO + H_2O \rightarrow CO_2 + H_2$).[8] Stoichiometrically, about 5.5 tons of $CO_2$ is produced per ton of $H_2$. This number is higher when accounting for the carbon cost of heating the steam.

Fortunately, 5.5 tons or more of carbon dioxide did not billow out of hydrogen plants in 2021 because of the availability of carbon-capture systems, which typically aim to capture about 90% of carbon dioxide emissions.[7,9] However, carbon-capture systems increase the cost of production of hydrogen gas. For both coal gasification ($1.34/kg $H_2$) and steam

methane reformation ($2.08/kg $H_2$), carbon-capture systems come with a premium of 19¢ per kilogram of $H_2$,[7] or a net premium of $14.7 billion for the 82% of the hydrogen gas produced in 2021. In the carbon neutral method of electrolysis, however, the premium is even higher ($5 to $6/kg $H_2$), with the 8.46 million tons of hydrogen gas having an associated cost of at least $42.3 billion.[7]

Evidently, environmental consciousness is not an economic business model. Despite its great potential to decarbonize the energy sector, the expensive hydrogen gas is no competition to the cheaper gasoline, which costs $1.49 per kilogram to produce in the United States.[10] Due to this extreme price difference, there is little incentive to move towards hydrogen as the main energy source at this moment. Considering the additional overhead cost associated with the initial planning and construction of a novel infrastructure for high-pressure hydrogen gas, investors will be reluctant to undertake such an ambitious change unless 1) the cost of hydrogen production reaches competitive prices, and 2) GHG emissions in hydrogen production reaches near zero. Thus, finding a cheaper yet carbon-neutral method of producing hydrogen gas is an imperative step toward building a carbon-neutral future with hydrogen.

*1.3. Nature's solution: hydrogenases*

In 1928, *Penicillium notatum* spores contaminated Dr. Alexander Fleming's *Staphylococcus aureus* colonies and began lysing them.[11,12] Noting this peculiar phenomenon, Dr. Fleming accidentally stumbled upon penicillin, which revolutionized the medical sciences as the first antibiotic. Dr. Fleming's story is one of the many examples of finding the solutions to modern problems in nature. After eons of evolution, it is not

surprising that nature has found solutions to most—if not all—problems imaginable, and hydrogen production is no exception.

Unlike steam methane reforming, first reported by Neuman and Jacob in 1924, which requires extreme temperatures and complex catalysts to enhance hydrogen yield,[13] hydrogenases, an enzyme first described by Kaserer in 1909,[14] catalyze the reversible oxidation of molecular (diatomic) hydrogen to protons and electrons with minimal overpotential in far more mild conditions of slightly acidic water of 20 °C to 100°C.[15,16,35]

$$H_2 \rightleftharpoons 2H^+ + 2e^- \quad (1)$$

Mostly found in anaerobic environments, where hydrogen may be a substantial supplier of the organism's energy,[17] hydrogenases are distinguished by their active site identities: [NiFe], [FeFe], and [Fe].[18,19] Hydrogenases have been shown to exhibit in vitro $H_2$ production rates of 1000 $s^{-1}$ with several [FeFe]-hydrogenases boasting rates of 10,000 $s^{-1}$. [18,20-22]

In particular, [NiFe]-hydrogenases contain active sites tuned by soft (polarizable) cyanide, carbon monoxide, and cysteine ligands (Figure 3).[18] The electronic tuning from these ligands facilitates the η-$H_2$ bond to the nickel atom and is further stabilized by synergistic interactions between $H_2(\sigma)/Ni(d_\sigma)$ and $H_2(\sigma^*)/Ni(d_\pi)$.[18,23] Following the binding event, the diatomic hydrogen was evidenced, though never directly observed to be heterolytically cleaved (equation 2) in the active site by H/D exchange experiments, where hydrogenase produced $^2$HH (hydrogen deuteride) species in the presence of $H_2$ and $D_2O$.[18,24,25]

$$H_2 \rightleftharpoons H^+ + H^- \quad (2)$$

*1.4. Pyrococcus furiosus soluble hydrogenase I*

This thesis focuses on a particular [NiFe]-hydrogenase found in *Pyrococcus furiosus*, a hyperthermophilic archaeon found in volcanic marine sediments: soluble hydrogenase I (*Pf* SH1). *Pf* SH1 is a tetrameric [NiFe]-hydrogenase (Figure 1) that is one of two of the archaeon's cytoplasmic hydrogenases and is responsible for 90% of the organism's molecular hydrogen production.[26,35]

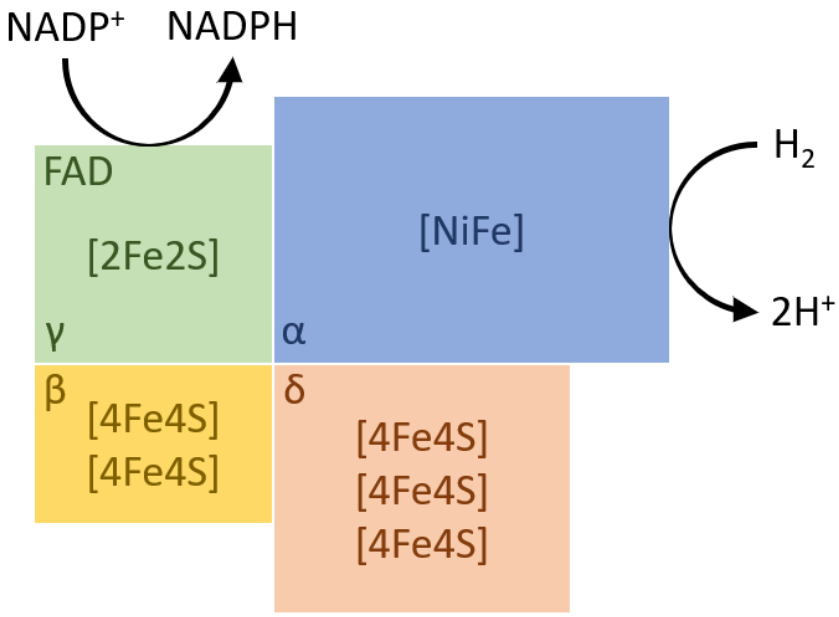


Figure 1. A diagram depicting the tetrameric form of *Pf* SH1. The α (large) and δ (small) subunits are the two typical subunits that make up all other [NiFe]-hydrogenases. This figure was adapted from reference 35.

The active site, hydrophilic proton transfer network, and hydrophobic gas channel are housed in the large subunit, whereas the small subunit contains the electron transport chain. The electron transport chain is comprised of three (proximal, medial, and distal) [4Fe4S] clusters. To illustrate the construction of the large and small subunits, the crystal structure of

an analogous [NiFe]-hydrogenase from the Miyazaki F strain of *Desulfovibrio vulgaris* (*Dv* MF, PDB: 4U9I) is illustrated in lieu of the yet to be crystalized *Pf* SH1 (Figure 2).

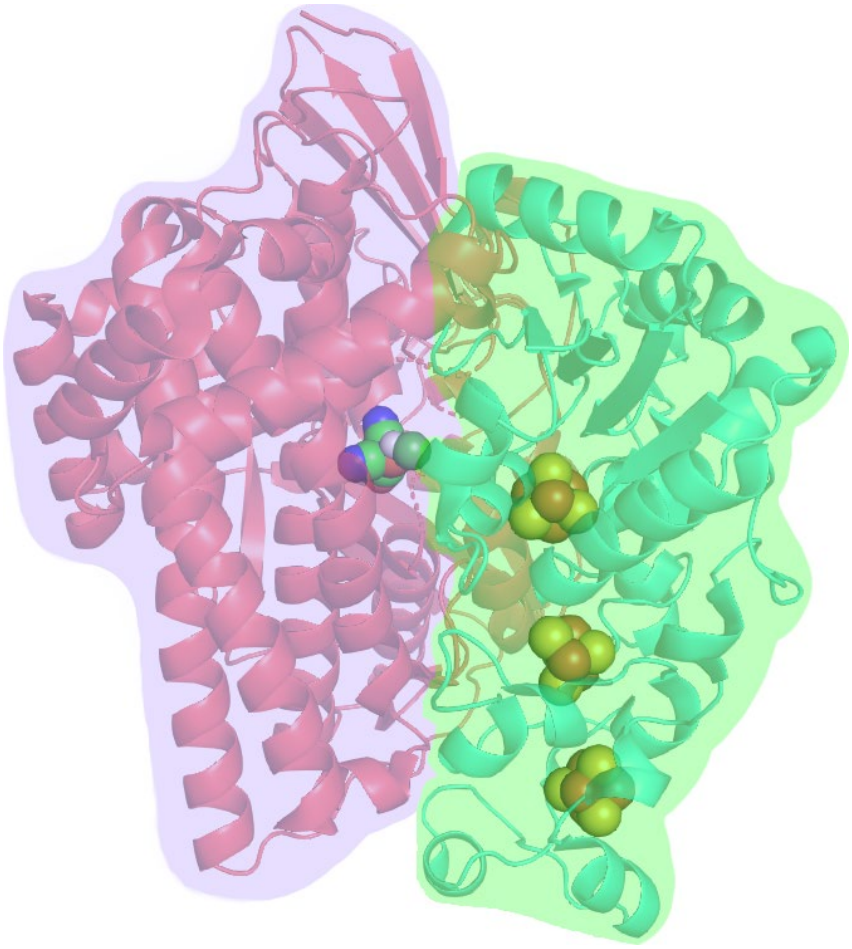

Figure 2. The crystal structure of a dimeric [NiFe]-hydrogenase from the Miyazaki F strain of *Desulfovibrio vulgaris* (*Dv* MF, PDB: 4U9I). The large subunit (magenta) houses the active site, hydrophilic proton transfer network, and hydrophobic gas channel (water and gas channels not highlighted). The small subunit (green) houses the electron transport chain with proximal (top-most), medial (middle), and distal (bottom-most) [4Fe4S] clusters. Generated with PyMOL.

The protons, electrons, and $H_2$ involved in the catalytic turnover are supplied by the proton transfer network, electron transport chain, and gas channel, respectively. The catalytic cycle of a [NiFe]-hydrogenase adapted from the Ph.D. dissertation of a former Dr. R. Brian Dyer laboratory member, Dr. Vansuch, is illustrated below (Figure 3).[18]

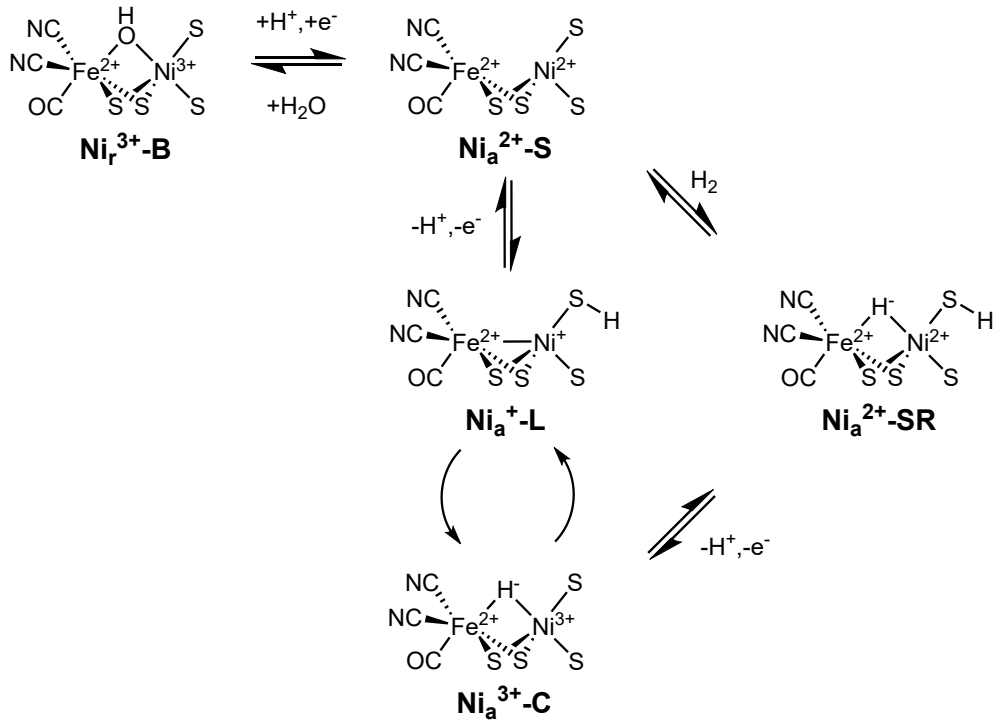


Figure 3. The catalytic cycle of a [NiFe]-hydrogenase. Sulfur atoms of catalytic cysteine residues and the soft CO/CN ligands tune the active site. The nomenclature follows the formal redox state of the active site nickel (iron remains in a low-spin configuration with an oxidation state of +2). Subscripts r is 'ready' and a is 'active'. The B state is an inactive form, S is the resting state, SR is the most reduced state, and L and C states are tautomeric forms of one another. The 'ready' inactive (oxidized) form, $Ni_r^{3+}$-B, occurs with exposure to oxygen and can be re-activated by hydrogen reduction in the order of minutes. Generated with ChemDraw.

Following the direction of $H_2$ production (counter-clockwise) from the resting state, the sulfur atom is protonated by another catalytic cysteine residue and the $Ni^{2+}$ is reduced to $Ni^{+}$ in a concerted proton-coupled electron transfer (PCET) event to form the $Ni_a^{+}$-L state. The L state then tautomerizes into the $Ni_a^{3+}$-C state, where a hydride transfer event occurs to a bridging position between the two metal atoms. Then, another PCET event forms the $Ni_a^{2+}$-SR state, at which point the thiolate proton couples with the bridging hydride to yield $H_2$.[18,27-29] Of course, the reverse reaction, hydrogen oxidation (equation 2) can also occur in the clockwise direction.

Despite the wealth of information presented thus far, much remains to be elucidated before the full potential of hydrogenases can be harnessed for hydrogen production. Fine mechanistic and functional details of the protein scaffold that tune the active site (second coordination sphere) remain unclear, and more progress is required to develop biomimetic catalysts that will replicate or surpass the unparalleled efficiency of hydrogenases in terms of $H_2$ production.[18,30] Currently, hydrogenase biomimetics suffer from high overpotential, oxygen sensitivity, low water solubility, and aggregation.[21] In one notable case, Brezinski and coworkers were able to synthesize a novel metallopolymer [FeFe]-hydrogenase mimetic with poly(2-dimethyl aminoethyl methacrylate) 'grafted' onto the [FeFe] active site which boasted low overpotential, oxygen insensitivity, water solubility, aggregation-resistant properties, and an impressive $H_2$ production rate of 250,000 $s^{-1}$.[21,31]

Although the true potential cannot be gauged without the full functional details of all coordination spheres of the enzyme, it is of great interest to fully characterize hydrogenases with the prospect of optimizing the enzyme and its mechanistic principles beyond the first coordination sphere as done by Brezinski and coworkers.

*1.5. The proton transfer chain*

To this end, this thesis aims to investigate the second coordination sphere around the [NiFe] active site of *Pf* SH1 with particular attention to the glutamic acid residue (E17, *Pf* SH1 numbering) positioned adjacent to the terminal cysteine residue. This residue was chosen due to its high degree of conservation, position, and strong evidence of involvement in proton transfer during catalysis as confirmed by cryogenic Fourier-transform infrared spectroscopy and electron paramagnetic resonance studies.[18,32,33] In addition to the

spectroscopic evidence, the location of the E17 residue bolsters the hypothesis of its involvement in the proton transfer chain. To illustrate this, the relevant proton/electron transfer faculties in *Dv* MF, which conserves the glutamic acid of the L0 motif, are depicted below (Figure 4).[18,37]

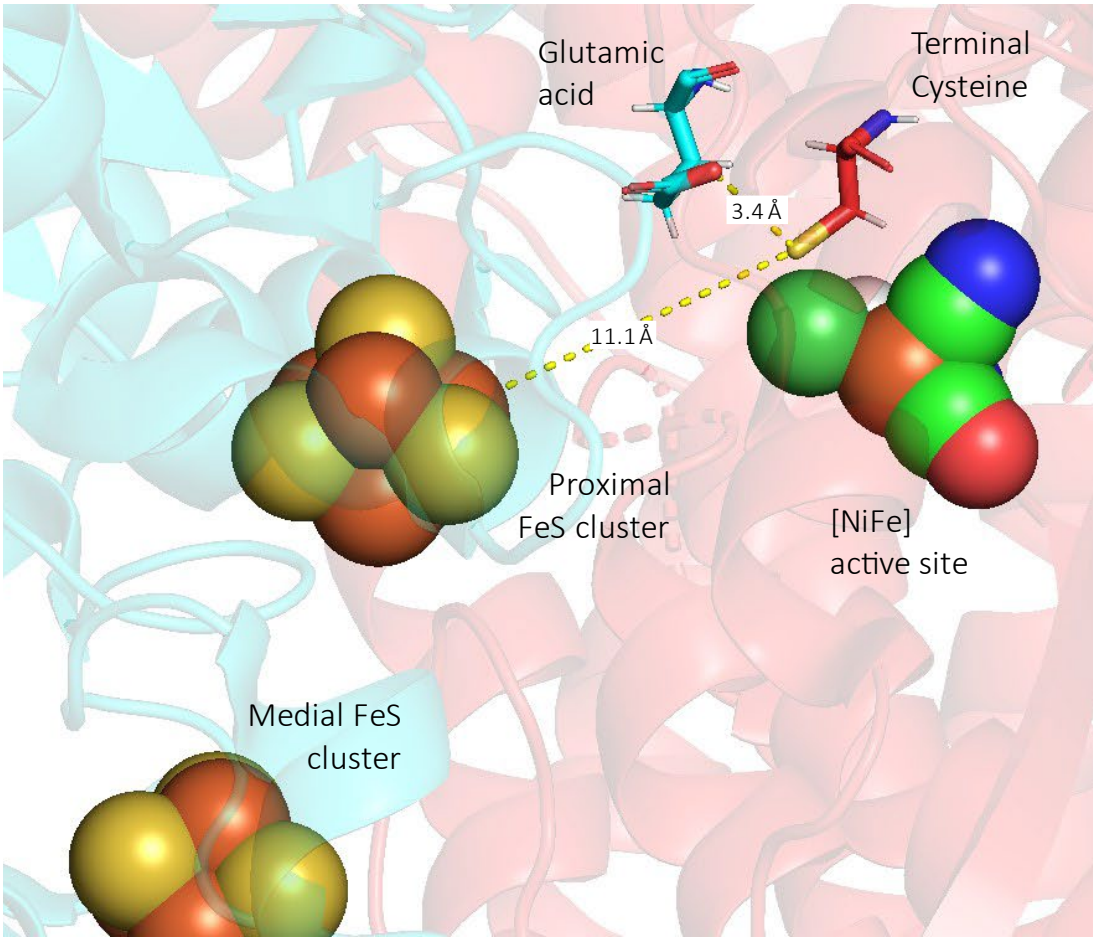


Figure 4. An overview of the key components of the proton/electron transfers in *Dv* MF. The glutamic acid and the terminal cysteine are a part of the proton transfer chain with 3.4 Å between the two proton-transferring residues. The terminal cysteine also participates in electron transfer with the proximal FeS cluster during a PCET event. Generated with PyMOL.

*1.6. The glutamic acid residue's far-reaching effect*

With ample evidence of the E17 residue's involvement in the proton transfer chain (PTC), two variants with a point mutation at this position were expressed by our collaborators at Dr. Michael W. W. Adams' laboratory in the Department of Biochemistry and Molecular Biology at the University of Georgia (section 2.2).

The first of the two mutations, E17D, substitutes aspartic acid for glutamic acid. Aspartic acid has a side chain that is one carbon shorter than that of glutamic acid. Thus, this point mutation increases the distance between the ionizable side chain and the sulfur of the adjacent terminal cysteine, resulting in reduced proton transfer efficiency without completely breaking the PTC. Hampered activity is expected from this reduced efficiency. The second mutation, E17Q, replaces glutamic acid with glutamine, effectively replacing the carboxylic acid moiety with an amide moiety. Thus, ionizability is lost in physiological pH ranges, resulting in a severed PTC and no expected activity.

The expected activity changes were consistent with a mutagenesis study carried out by Dementin and coworkers, with no activity being observed by an E/Q variant of a [NiFe]-hydrogenase from *Desulfovibrio fructosovorans*.[33] However, Dr. Vansuch saw about 4% activity in the E17D *Pf* SH1 variant. The discrepancy in findings only grew in the E/Q mutation, where Szőri-Dorogházi and coworkers reported about 50% activity in *a hydrogenase from Thiocapsa roseopersicina*, Dr. Vansuch about 10% activity in *Pf* SH1, and Armstrong and coworker about 1% activity in a hydrogenase from *Escherichia coli.*[18,36,38]

The various species had conserved glutamic acid residue at the E17 position,[18] but a mutation of this residue was handled differently in each. This inconsistency suggests that the protein scaffold impacts the catalytic properties of hydrogenases. Furthermore, it seems that the E17 residue is involved in more than just the PTC as simple mutations that decrease the efficiency of the PTC or remove the ionizability of the glutamic acid residue impacts the enzymes in unexpected ways. It follows that the secondary coordination sphere, where the E17 residue resides, is involved in more than what meets the eye.

To gain insight into the role of the glutamic acid residue, the two variants—E17D and E17Q—were examined in equilibrium, and kinetic studies were carried out via Fourier-transform and transient absorbance infrared spectroscopy, respectively.

# Chapter 2. Temperature-Dependent Auto-Oxidation

## *2.1. Motivation*

Recall that the $H_2$ oxidation reaction (equation 1) occurs in the clockwise direction of the catalytic cycle of *Pf* SH1 (Figure 3). Since the oxidation reaction is endothermic, if the temperature of the environment is increased, the equilibrium is expected to shift to the right according to Le Chatelier's principle. It follows that the catalytic cycle will be pushed in the clockwise direction with increasing temperature, thereby shifting the equilibrium distribution of states. And as proton transfer is an essential mechanism in the catalytic cycle, a comparison of the wild type (WT), E17D, and E17Q variants should provide insight into how the E17D and E17Q mutations affect the PTC.

So, in this experiment, aptly named temperature-dependent auto-oxidation (TDEP), the equilibrium population distribution will be monitored via FT-IR at incrementally increasing temperatures to observe the differences that the perturbed PTC will cause.

*2.2. Materials*

The buffer used to prepare the sample and serve as the reference for FT-IR measurements, referred to as TDEP buffer, is a solution of 50 mM HEPPS (MP Biomedicals) at a pH of 8.52. This buffer was prepared in the open atmosphere with deionized water and pH-adjusted with hydrochloric acid or sodium hydroxide. The pH of the buffer was monitored by a benchtop pH meter (AE150, Fisher Scientific) with an uncertainty of ± 0.05 pH units. The buffer solution was then filtered through a 0.2 µm sterile syringe filter (Corning) to remove any bacteria that may have been introduced during the preparation. The prepared buffer was then taken into the anaerobic glove box to be bubbled with the glove box's atmosphere via a contained fish pump for 30 minutes to purge the dissolved oxygen from the solution. The introduction of impurities during the box purge was avoided by attaching another 0.2 µm filter and an 18G sterile hypodermic needle to the pump tubing.

The stocks of the *Pf* SH1 WT/E17D proteins used for TDEP experiments were prepared by our collaborators, Chang-Hao "Perry" Wu and Dominik Haja from Dr. Michael W. W. Adams' laboratory in the Department of Biochemistry and Molecular Biology at the University of Georgia, and the detail of the synthesis is reported by a former lab member, Dr. Vansuch, in his Ph.D. dissertation.[18]

Before TDEP experiments, a calculated volume of the protein stock was buffer exchanged into the TDEP buffer by centrifuging the stock and the TDEP buffer in a low volume 50 kDa molecular weight cut-off filter (Millipore) at 10,000 rpm for 5-8 minutes at least 6 times. Then, the buffer exchanged stock was concentrated down to about 20-25 µL at 11,000-12,000 rpm for 5-10 minutes. The concentrated, buffer-exchanged stock was then contained in a low-volume, gas-tight vial (Phenomenex) to be taken out of the anaerobic glove box and its headspace was purged with $N_2/H_2$ mix (95%/5%, Select Gas) for 30 minutes using an air-tight purging system devised by Dr. Vansuch. To purge, 26G x ½ (0.45 mm x 13 mm) hypodermic needles (BD PrecisionGlide™) were used as both the vent and purge needle. The final volume of the concentrated, buffer-exchanged, $H_2$-purged stock was around 15 µL to 20 µL and had an enzyme concentration of ~500 µM.

With all materials prepared, the infrared (IR) cell for TDEP experiments was put together in an anaerobic glove box (Coy Laboratory Products) with an atmosphere of primarily $N_2$, >8 ppm of $O_2$, and ~1% $H_2$ (Select Gas) verified by $O_2$ and $H_2$ sensors present in the anaerobic glove box.

*2.3. Method*

*2.3.1. IR cell preparation for FT-IR spectroscopy*

The IR cell was constructed in a similar construction as shown in appendices A and B with a drilled $CaF_2$ window in place of the $CaF_2$ window below the butyl rubber. The IR cell was sealed by applying high-temperature vacuum grease (Apiezon H grease) to the Teflon spacer. In the anaerobic glove box, 26G x ½ (0.45 mm x 13 mm) hypodermic needles were inserted at the top two ports. Then, the sample side was injected with ~500

μM of *Pf* SH1 WT/E17D in TDEP buffer and the reference side was injected with the same buffer from the bottom two ports using a gastight syringe (Hamilton) in the anaerobic glove box. Then, set screws were promptly screwed into place with a small bead of Apiezon H grease applied to its threading to completely seal the IR cell.

*2.3.2. FT-IR instrumentation preparation*

The prepared IR cell was then mounted on the stage of the desiccate chamber (Appendix C) of the Varian 660 Fourier-transform Infrared spectroscope and the chamber was allowed 10-30 minutes to purge most of the water vapor out of its box atmosphere.

*2.3.3. FT-IR data collection*

Then, a LabVIEW program written in-house was used to collect FT-IR spectra of the sample and the reference from around 10 °C to 55 °C in increments of 5 °C via the Resolutions Pro FT-IR software from Varian. Some temperatures have been omitted due to gross errors.

At each temperature increment, the sample was allowed 10 minutes to equilibrate with the water bath's temperature, and 1024 (WT) or 128 (E17D) scans were taken to be co-added for 10 cycles in Resolutions Pro. The ten FT-IR spectra were then averaged and assigned as the FT-IR spectrum for that temperature.

## *2.4. Results and Discussion*

### *2.4.1. FT-IR data processing*

The single beam spectra collected by the Resolution Pro software of the sample solution were ratioed with that of the reference solution according to equation 3 to obtain the absorbance spectra.

$$Absorbance = -\log\left(\frac{I_{enzyme}}{I_{reference}}\right) \quad (3)$$

Where $I_{enzyme}$ and $I_{reference}$ are the MCT detector signal of the IR beam passing through the sample and reference solution, respectively. A conservative sum of 5 points spline correction was applied throughout the regions of 1860-1910 $cm^{-1}$, 1970-2030 $cm^{-1}$, and 2100-2200 $cm^{-1}$. The processed absorbance spectrum at each temperature was then subtracted from the coldest temperature's spectrum to create a difference spectrum over the temperature range, which is graphed with Igor Pro (Figures 4 and 5).

### *2.4.2. TDEP difference spectra*

The peak assignments referred to in this section are described in Dr. Vansuch's Ph.D. dissertation.[18] In the difference spectra of the WT shown below (Figure 5), the ~2 mOD bleach at 1966.1 $cm^{-1}$ corresponds to the $Ni_a^{3+}$-C state, the ~0.5 mOD broad growth to $Ni_r^{3+}$-B, and the larger growth of ~1 mOD at 1949.7 $cm^{-1}$ to the resting state, $Ni_a^{2+}$-S. Though there are more peaks visible in the spectra to the right of 1940 $cm^{-1}$, the identification and implication of these peaks are beyond the scope of this thesis.

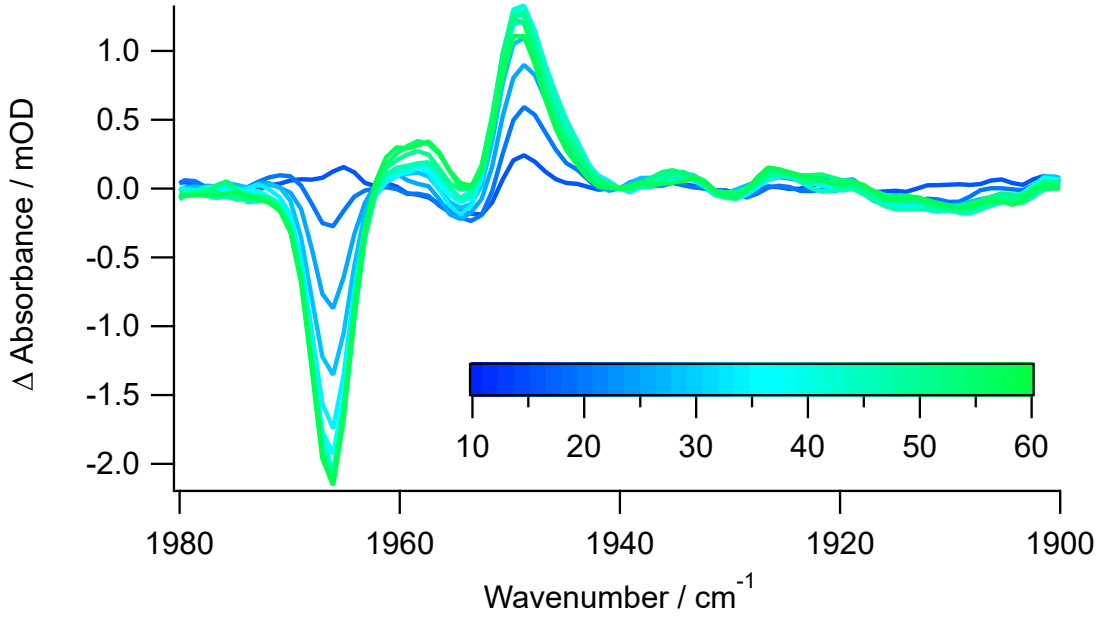


Figure 5. The baseline corrected difference spectrum (zeroed at 1940 $cm^{-1}$) of the WT of *Pf* SH1. There is a decrease in absorbance at 1966.1 $cm^{-1}$, a small increase at 1957.4 $cm^{-1}$, and a large increase at 1948.7 $cm^{-1}$.

This bleach of C along with the broad growth of B and the larger growth of the S states is consistent with a shift of the catalytic cycle in the clockwise direction. This trend is consistent with the C state tautomerizing into the L state and reforming the resting state. The small growth of the B state can be attributed to oxygen contamination in the IR cell as the experiment progresses.

On the other hand, in the difference spectra of the E17D variant shown below (Figure 6), a bleach of ~1 mOD can be seen at 1937.1 $cm^{-1}$ adjacent to the ~0.5 mOD growth at 1929.4 $cm^{-1}$.

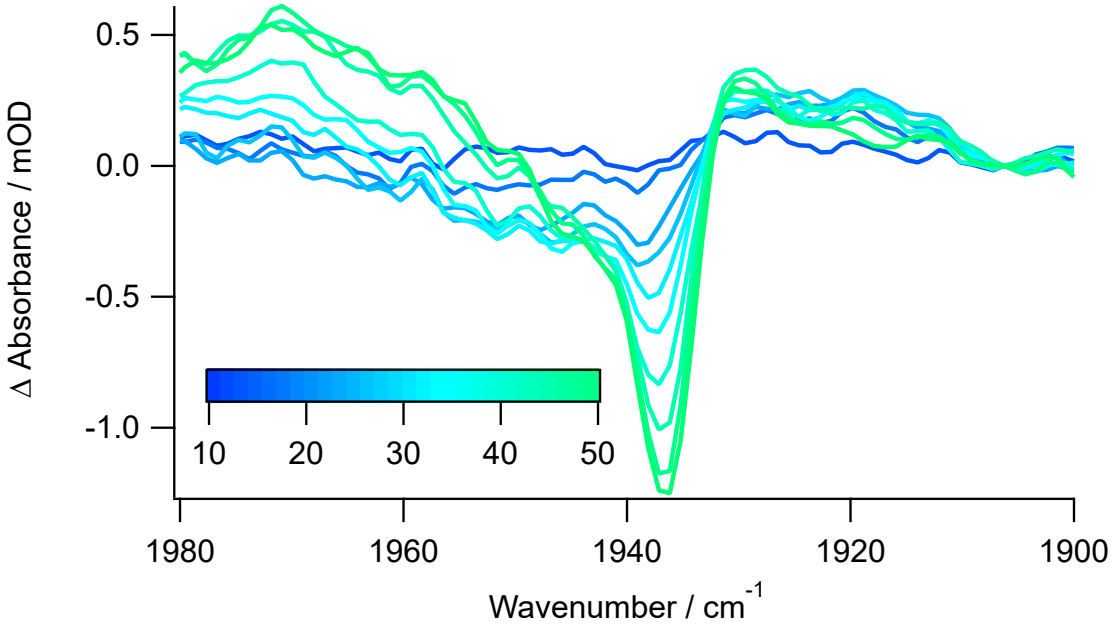


Figure 6. The baseline corrected difference spectrum (zeroed at 1906.3 $cm^{-1}$) of the E17D variant of Pf SH1. There is a large decrease in absorbance at 1936.2 $cm^{-1}$ and a small growth at 1929.4 $cm^{-1}$.

The difference spectra of E17D seem to be consistent with that of the WT except for the absence of a large growth which was that of the S state in WT. The only bleach in the range is a bleach of about 1 mOD at 1936.2 $cm^{-1}$. This can be attributed to the bleach of the C state even though it is ~30 $cm^{-1}$ redshifted. This assignment is consistent with the fact that the small increase of the B state is also redshifted by about 30 $cm^{-1}$. The E/D mutation can have a drastic effect on metalloenzymes, so this large redshift can be attributed to this E/D mutation.[18] However, another difference in the E17D mutation is the fact that no large growth is seen to complement the bleach of the C state. If the only effect of the E17D mutation was the redshift of about 30 $cm^{-1}$, a growth of the S state should be seen around 1927 $cm^{-1}$. However, this expected growth of the S state is not seen in the difference spectrum of the E17D variant.

*2.5. Conclusion*

From the TDEP data of WT and E17D, it seems that the E17D mutation has changed the spectroscopic properties of *Pf* SH1 beyond simply perturbing the proton transfer chain. While the WT showed growths and bleaches consistent with the clockwise direction of the catalytic cycle, the E17D mutant did not show the expected activity. The TDEP data of the E17Q mutant can be seen in Dr. Vansuch's dissertation, where the E17Q expectedly shows no activity with no growths or bleaches to be found in the range of CO stretches.

In sum, the WT and E17Q variant exhibited expected activity while the E17D mutant showed unexpected effects on the catalytic properties of *Pf* SH1. The lack of a growth peak to complement the ~1 mOD bleach of the C state may point to the fact that the E17D enzyme had degraded over the course of about two years of it being in storage, or the E17D mutation may have far greater effects on the spectroscopic properties of the enzyme such that the corresponding growth peak is outside of the range of interest. Due to significant baseline drifting in the range outside of 1980-1900 $cm^{-1}$, more TDEP data must be collected for the E17D mutant to elucidate what may be going on.

As such, it would be interesting to investigate the catalytic landscape of the E17D variant with 1) additional TDEP experiments without a major baseline shift, and 2) increase the concentration of the sample to amplify small peaks that may be growing in its spectra so that the complementary growth from the large C bleach may be elucidated further.

# Chapter 3. CO Incubation and Photolysis

## *3.1. Motivation*

The crystallographic analysis done by Volbeda and coworkers on an analogous [NiFe]-hydrogenase from *Desulfovibrio fructosovorans* suggests that the E17 residue in *Pf* SH1 lines the wall of the gas channel near the active site.[1,34] This suggests that the identity of the E17 residue's influence may reach beyond the PTC. So, to probe this gas channel dynamic, CO can be used in place of $H_2$ to mimic the binding event at the active site nickel. This is possible because, in the transition from the $Ni_a^{2+}$-S (Ni-S) and the $Ni_a^{2+}$-SR states (Figure 2), an η-$H_2$ bond formation on the active site nickel is followed by heterolytic cleavage of the $H_2$ atom to form the SR state. So, if a CO molecule binds to the nickel in place of the $H_2$, then the hydrogenase will remain in a "Ni-SCO" state.

Taking advantage of CO's ability to form the Ni-SCO state, the CO incubation and photolysis (CO-IP) experiment has two aims. The first aim is to observe the exchange of enzyme population between the Ni-SCO and Ni-S, which will assist in assigning the Ni-S peak in the FT-IR spectrum. The second aim is to probe the possible effects of the identity of the E17 residue on the gas channel dynamics, which may be elucidated by the kinetics of the Ni-S decay/Ni-SCO reformation.

However, the timescale of the CO dissociation and binding events must be considered. CO dissociates from the nickel when flashed in the Ni-SCO state on the ultrafast (picosecond) timescale,[18] which is unattainable with currently available instrumentation. However, the CO binding event occurs in the microsecond timescale, which is attainable with the transient

absorbance infrared (TA-IR) instrumentation. Therefore, the CO-IP experiments will observe the recovery of the Ni-SCO peak.

*3.2. Materials*

The buffer used to prepare the CO-IP samples, referred to as the TA buffer, is a solution of 50 mM HEPPS (MP Biomedicals) at a pH of 8.50. The TA buffer was prepared in an identical manner as the buffer preparation described in section 2.2.

The stocks of the *Pf* SH1 E17D protein used for CO-IP experiments were prepared by Chang-Hao "Perry" Wu and Dominik Haja from Dr. Michael W. W. Adams' laboratory in the Department of Biochemistry and Molecular Biology at the University of Georgia, and the details of hydrogenase variant expression are reported by a former lab member, Dr. Vansuch, in his Ph.D. dissertation.[18]

Before CO-IP experiments, a calculated volume of the stock was buffer exchanged into the TA buffer by centrifuging the stock and the TA buffer in a low volume 50 kDa molecular weight cut-off filter at 10,000 rpm for 5-8 minutes at least 6 times. To ensure that CO is incorporated into the sample solution, the final buffer exchange was performed with TA buffer that was bubbled with CO for 30 minutes. The concentrated, buffer-exchanged stock was then transferred to a low-volume, gas-tight vial (Phenomenex), taken out of the anaerobic glove box and its headspace, and purged with carbon monoxide for 30 minutes. To purge, 27G x 1 ¼ (0.4 mm x 30 mm) hypodermic needles were used as both the vent and purge needles. The final volume of the concentrated, buffer-exchanged, CO-purged stock was around 15 µL to 20 µL and had an enzyme concentration of ~1 mM.

Just like the TDEP experiments (section 2.2), IR cells for TA-IR measurements were put together in the anaerobic glove box with an atmosphere of primarily $N_2$, >8 ppm of $O_2$, and ~1% $H_2$ verified by O2 and H2 sensors present in the anaerobic glove box.

*3.3. Method*

*3.3.1. IR cell preparation for TA-IR*

The IR cell was constructed as shown in appendices A and B. The unscrewed IR cell was brought into the anaerobic glove box with the high-temperature vacuum grease pre-applied to the Teflon spacer. Then, ~1 mM of *Pf* SH1 E17D in TA buffer and the TA buffer was deposited onto the $CaF_2$ window in a small line with a gastight syringe. The second $CaF_2$ window was then placed on top of the bottom $CaF_2$ window and screwed down in under 2-3 minutes. The same preparation was done on the benchtop with myoglobin for the control experiment.

*3.3.2. TA-IR instrumentation preparation*

The preparation of the transient absorbance infrared spectroscopy (TA-IR) instrumentation (Appendix D) for transient absorbance data collection involves three main steps: 1) visual alignment, 2) temperature-jump alignment, and 3) sample alignment.

First, during the visual alignment, a chopper is placed in front of the stage to allow for visualization of the magnitude of the IR signal, which is displayed by the computer oscilloscope software, GaGeScope. A 200 µm pinhole (Fort Wayne Wire Die Inc.) is mounted on the stage and aligned to the QCL beam such that the maximal signal is read

out on GaGeScope. Then, this process is repeated with a 50 µm pinhole. With the 50 µm pinhole aligned to the QCL beam, the chopper is removed, and the Nd:YAG beam is aligned to the 50 µm pinhole by finding the angle at which the beam splitter reflects the Nd:YAG beam such that the maximum amount of the beam passes through the pinhole.

The visual alignment provides a rough alignment of the pump (Nd:YAG) and probe (QCL) beams, but visual methods are limited in their precision, so the pump and probe beams are then aligned by finding the angle of the Nd:YAG beam splitter at which the magnitude of the detected temperature jump (t-jump) of water caused by the pump beam is greatest. To take snapshots of each flash, an external trigger was used to trigger both the data collection in the GaGeScope software and the shutter of the Nd:YAG laser head.

After finding the maximum magnitude of the t-jump signal, the prepared IR cell is mounted on the stage. Then, the QCL is set to a wavenumber of interest and the signal is checked with the optical chopper. To ensure experimental consistency, the amplitude of the peak is set to about 1 V by modulating the infrared signal via polarizers.

*3.3.3. Transient absorbance data collection*

To collect the transient absorbance data, a LabVIEW program written in-house was used. The voltage signal of the MCT detector is first zeroed by modulating the polarizers. With the IR signal zeroed, the voltage readout from the MCT detector is converted into absorbance via the LabVIEW program. Then, the sample is flashed with the 10-nanosecond pulse Nd:YAG pump beam 10-30 times, and the transient absorbance data

from each flash is averaged. This process was repeated for each wavenumber to be measured. The acquisition properties of the data collection are shown below (Table 1).

| | |
|---|---|
| Sampling rate | 25 MHz |
| Pre-trigger points | 100 |
| Post-trigger points | 4.00E+06 |
| Coupling | DC |
| Impedance | 50 Ohm |
| Range | ± 1 V |
| Scans to average | 1000 |
| Resolution | 2.00E-08 |

Table 1. A table of select acquisition properties used in the LabVIEW program written in-house for TA-IR experiments. The pre-trigger and post-trigger points refer are terms relative to the "triggered" flash of the 532 nm Nd:YAG beam.

### *3.4. Results and Discussion*

#### *3.4.1. TA-IR data processing*

The LabVIEW program written in-house records light and dark scans and then subtracts the dark voltage from the light voltage. This voltage difference is then converted to absorbance. Hence, the units of the transient absorbance traces are changes in absorbance (Δ absorbance).

With each flash of the pump laser, a temperature jump is induced in the sample solution, causing a t-jump signal. So, this t-jump signal must be subtracted from each wavelength to isolate the bleach that occurs from the Ni-CO dissociation. To this end, the cooling signature, or the overall t-jump signal including the ramp down to zero absorbance as the solution relaxes, is taken from 1914-1910 $cm^{-1}$ and subtracted from all

transient absorbance traces at each wavenumber. The 1914-1910 range was chosen as no relevant activity is expected at this range.

Finally, to visualize the spectroscopic landscape of the Ni-S and Ni-SCO peaks, a "time slice" of the t-jump subtracted transient absorbance traces are plotted. In a time slice, the 'ΔΔ absorbance' of all t-jump subtracted transient absorbance traces is plotted against their respective wavenumbers at a specific time point.

*3.4.2. Transient absorbance traces*

The CO-IP experiment's protocol was validated with a control experiment of CO-incubated myoglobin (Figure 7) to ensure that CO photolysis can be observed via TA-IR. The CO dissociation can be seen by the large bleach that occurs in the microsecond timescale, and the subsequent recovery is seen. The successful observation of Mb-CO recovery validates that the method can observe CO photolysis in a solution via the TA-IR instrumentation after appropriate sample preparation.

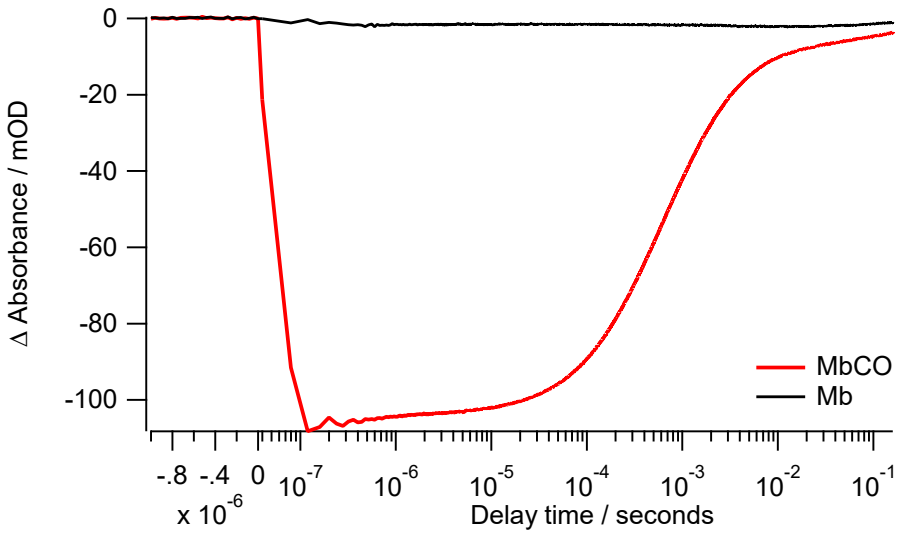


Figure 7. The transient absorbance trace of CO-incubated myoglobin (6 mM) sample at 1943 $cm^{-1}$. In the split x-axis, the negative pre-trigger seconds are graphed in a linear scale and the positive post-trigger points (delay time) are in a logarithmic scale. The recovery of the large bleach caused by CO dissociating from myoglobin can be seen.

However, when the CO-IP experiment was carried out with the E17D variant of *Pf* SH1, only cooling signatures of the sample solution is present from 1910 to 1968 $cm^{-1}$.

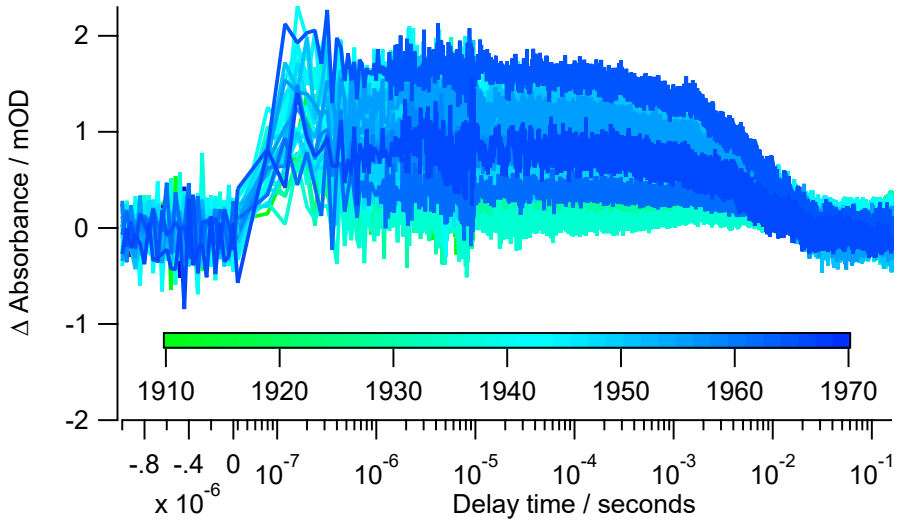


Figure 8. The transient absorbance traces of CO-incubated E17D from 1910 to 1968 $cm^{-1}$. The range is covered mostly with a resolution of 1 $cm^{-1}$. In the split x-axis, the negative pre-trigger seconds are graphed in a linear scale and the positive post-trigger points (delay time) are in a logarithmic scale.

The t-jump subtracted transient absorbance traces are shown below (Figure 9), but as shown in the time slice (Figure 10), no Ni-SCO or Ni-S peaks can be discerned above the noisy background signal.

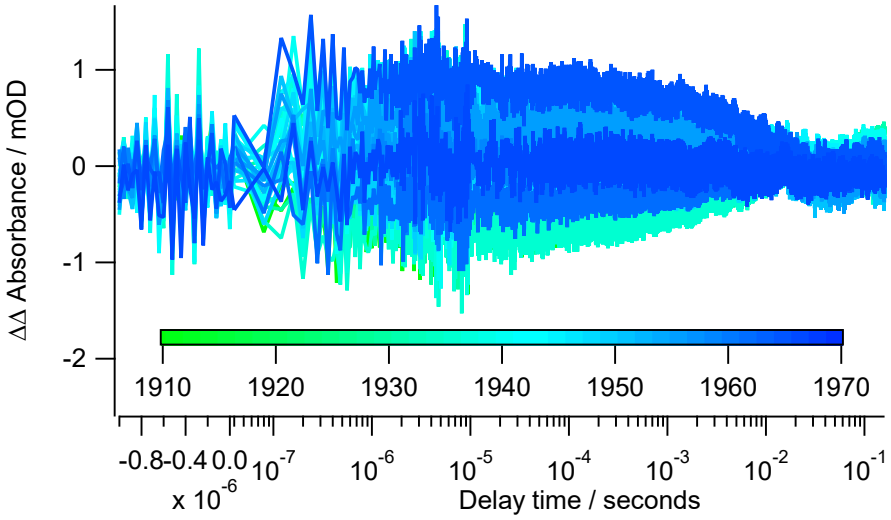


Figure 9. Temperature-jump subtracted traces. In the split x-axis, the negative pre-trigger seconds are graphed in a linear scale and the positive post-trigger points (delay time) are in a logarithmic scale.

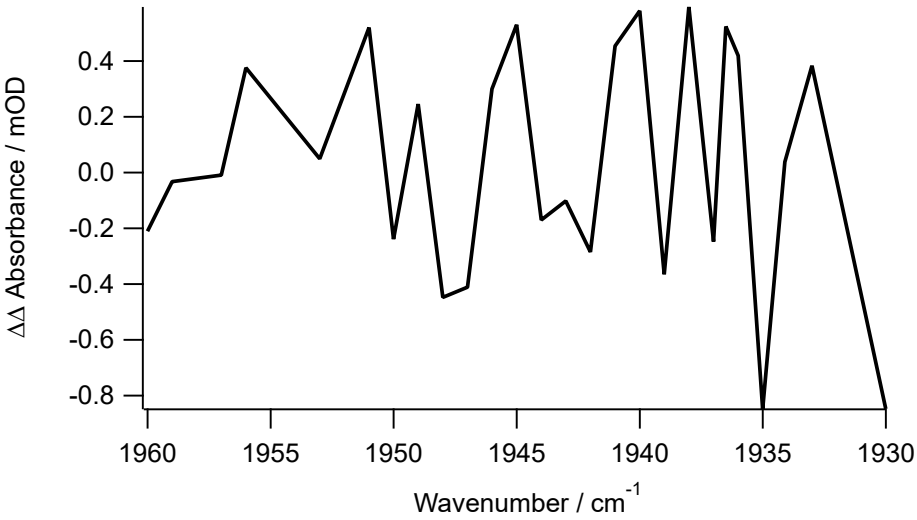


Figure 10. A time slice of the t-jump subtracted traces at 15 µs. In the split x-axis, the negative pre-trigger seconds are graphed in a linear scale and the positive post-trigger points (delay time) are in a logarithmic scale.

This is unexpected because the shifting of peaks was observed in the TDEP experiment of E17D (Figure 5, section 2.4.2), which would suggest that the enzyme did have catalytic activity.

*3.5. Conclusion*

With the instrumentation and the CO-IP experiment methodology validated by the myoglobin control experiment, CO photolysis was unable to be observed for the E17D variant. There are a couple of possibilities as to why no bleach was observed by the dissociation of CO.

First, CO may not have sufficiently been dissolved into the sample solution during preparation. Despite efforts such as buffer exchanging the final spin with CO-bubbled TA buffer and allowing less than 30 seconds of the CO-purged sample solution to be exposed to the anaerobic glove box's atmosphere, it is still possible that CO was not sufficiently dissolved in the concentrated sample solution.

Second, the E17D stock may have been inactivated by oxygen. The E17D stocks used in this CO-IP experiment were shipped by the collaborators in April 2021 and the protein samples may have been inactivated over the course of two years. And since the Ni-S form is required for the CO molecules to bind at the nickel to observe the Ni-SCO state, inactivation of the enzyme may have prohibited the CO from binding to the nickel.

If the CO photolysis can be observed through future CO-IP experiments for the WT, E17D, and E17Q variants, the impact of the E17 mutations on the gas channel dynamics as well as the Ni-S phase shift may be elucidated.

# Appendix

## *Appendix A. Exploded view of an IR cell*

The IR cell is constructed of custom-made copper plates holding together two $CaF_2$ windows separated by a 67.2 µm Teflon spacer and padded by butyl rubber and Teflon. An exploded view of the IR cell is shown below (Figure A).

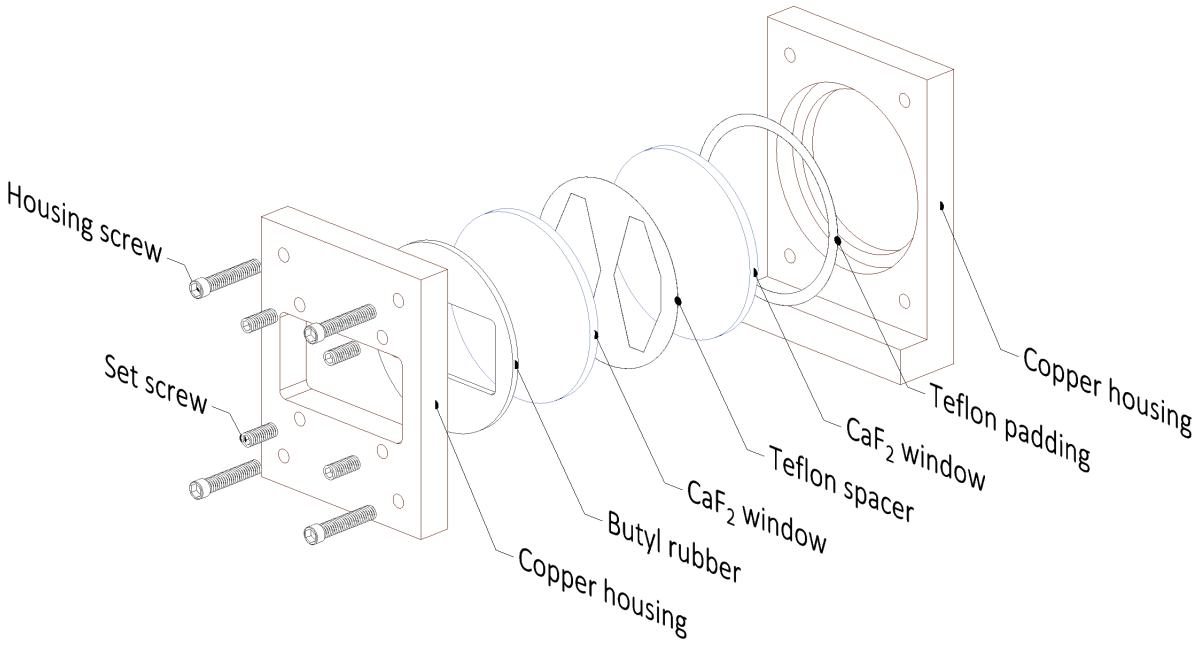


Figure A. An exploded view of the IR cell used for Fourier-transform and transient absorbance infrared spectroscopy experiments. This illustration was created with Autodesk Inventor.

*Appendix B. IR cell assembly*

The assembly of an IR cell is shown below (Figure B).

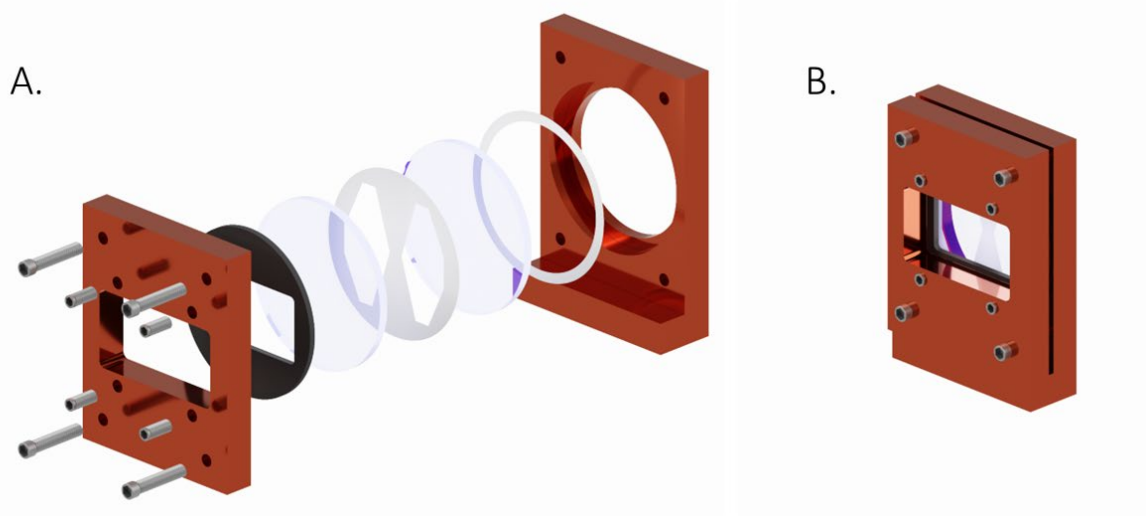


Figure B. (A) Illustration of a rendered exploded view. (B) An assembled view. The $CaF_2$ windows are tinted blue for visibility but are transparent under white light.

*Appendix C. Fourier-transform infrared spectrometer desiccate chamber*

To mitigate the water vapor peaks that would obfuscate the mOD-scale peaks from the hydrogenase samples, an external desiccate chamber was built next to the Varian 660 FT-IR spectrometer. Water vapor was removed in this chamber by vacuuming the air out of the chamber while constantly supplying dry air into it. Following the beam from the exit hole of the Varian 660 spectrometer, a gold parabolic mirror (GPM) reflects the infrared beam to the sample, which is re-collimated by a second GPM and a third GPM directs the beam to the liquid nitrogen-cooled Mercury-Cadmium-Telluride (MCT) detector (Kolmar). Used to move the sample for FT-IR experiments, the water-circulated copper sample stage is fixed to a stepping motor drive (Mark-102, Sigma Koki).

*Appendix D. Transient absorbance infrared instrumentation diagram*

The TA-IR instrumentation was designed and created by previous postdoctoral fellows in the Dyer laboratory, which is shown below (Figure D).

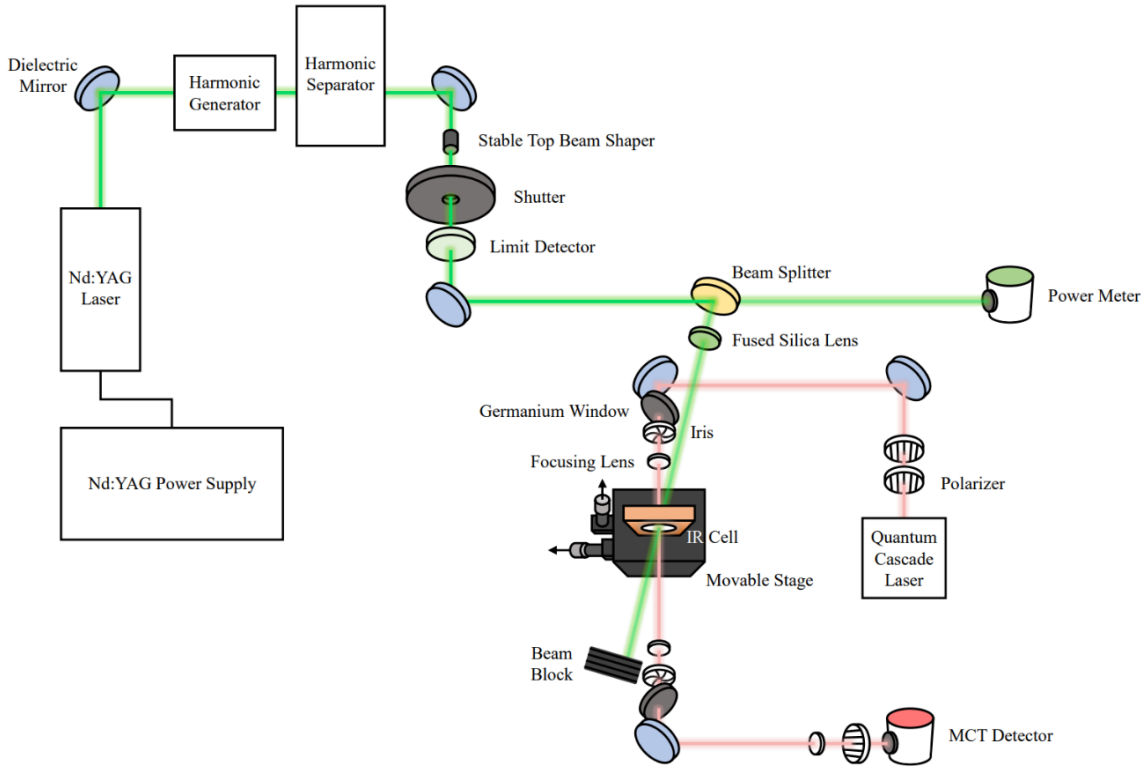


Figure D. A diagram of the transient absorbance infrared spectroscopy instrumentation. The Surelite neodymium-doped yttrium aluminum garnet (Nd:YAG) laser (Continuum), with a fundamental frequency of 1064 nm, is passed through a harmonic generator and then through a harmonic separator to isolate the 2$^{nd}$ harmonic of 532 nm. The power of the Nd:YAG laser is monitored by splitting the beam in half at the beam splitter and directing the two beams to a power meter and the sample. The fused silica lens is used to focus the Nd:YAG beam. The quantum cascade laser (QCL) has a wavenumber range of 2010 cm$^{-1}$ to 1805 cm$^{-1}$. The polarizers are used to modulate the magnitude of the IR signal to avoid saturating the liquid nitrogen-cooled Mercury-Cadmium-Telluride (MCT) detector. The germanium windows allow the QCL beam to pass through while reflecting the 808 nm beam (not pictured) that is used as a guide beam in the context of this thesis. The focusing lenses are $CaF_2$ focal lenses and are used to focus the beam to a point where it contacts the contents of the IR cell, which is mounted on a copper stage. The irises assist in the alignment process of the instrument.

References

(1) Pörtne H.-O.; D.C. Roberts; H. Adams; I. Adelekan; C. Adler; R. Adrian; P. Aldunce; E. Ali; R. Ara Begum; B. Bednar-Friedl; R. Bezner Kerr; R. Biesbroek; J. Birkmann; K. Bowen; M.A. Caretta; J. Carnicer; E. Castellanos; T.S. Cheong; W. Chow; G. Cissé; S. Clayton; A. Constable; S. Cooley; M.J. Costello; M. Craig; W. Cramer; R. Dawson; D. Dodman; J. Efitre; M. Garschagen; E.A. Gilmore; B. Glavovic; D. Gutzler; M. Haasnoot; S. Harper; T. Hasegawa; B. Hayward; J.A. Hicke; Y. Hirabayashi; C. Huang; K. Kalaba; W. Kiessling; A. Kitoh; R. Lasco; J. Lawrence; M.F. Lemos; R. Lempert; C. Lennard; D. Ley; T. Lissner; Q. Liu; E. Liwenga; S. Lluch-Cota; S. Löschke; S. Lucatello; Y. Luo; B. Mackey; K. Mintenbeck; A. Mirzabaev; V. Möller; M. Moncassim Vale; M.D. Morecroft; L. Mortsch; A. Mukherji; T. Mustonen; M. Mycoo; J. Nalau; M. New; A; Okem (South Africa; J.P. Ometto; B. O'Neill; R. Pandey; C. Parmesan; M. Pelling; P.F. Pinho; J. Pinnegar; E.S. Poloczanska; A. Prakash; B. Preston; M.-F. Racault; D. Reckien; A. Revi; S.K. Rose; E.L.F. Schipper; D.N. Schmidt; D. Schoeman; R. Shaw; N.P. Simpson; C. Singh; W. Solecki; L. Stringer; E. Totin; C.H. Trisos; Y. Trisurat; M. van Aalst; D. Viner; M. Wairu; R. Warren; P. Wester; D. Wrathall; and Z. Zaiton Ibrahim; 2022: Technical Summary. [H.-O. Pörtner; D.C. Roberts; E.S. Poloczanska; K. Mintenbeck; M. Tignor; A. Alegría; M. Craig; S. Langsdorf; S. Löschke; V. Möller; A. Okem (eds.)]. In: Climate Change 2022: Impacts; Adaptation; and Vulnerability. Contribution of Working Group II to the Sixth Assessment Report of the Intergovernmental Panel on Climate Change [H.-O. Pörtner; D.C. Roberts; M. Tignor; E.S. Poloczanska; K. Mintenbeck; A. Alegría; M. Craig; S. Langsdorf; S. Löschke; V. Möller; A. Okem; B. Rama (eds.)]. Cambridge University Press, Cambridge, UK and New York, NY, USA, pp. 37-118, doi:10.1017/9781009325844.002.

(2) Kweku, D.; Bismark, O.; Maxwell, A.; Desmond, K.; Danso, K.; Oti-Mensah, E.; Quachie, A.; Adormaa, B. Greenhouse Effect: Greenhouse Gases and Their Impact on Global Warming. *Journal of Scientific Research and Reports* 2018, *17* (6), 1–9.

(3) Bailey, D. The effects of climate change. https://climate.nasa.gov/effects/ (accessed Mar 27, 2023).

(4) Hydrogen Basics. https://afdc.energy.gov/fuels/hydrogen_basics.html (accessed Mar 27, 2023).

(5) IEA. Hydrogen – analysis. https://www.iea.org/reports/hydrogen (accessed Mar 27, 2023).

(6) Kurtz, J.; Saur, G.; Sprik, S. Hydrogen Fuel Cell Performance as Telecommunications Backup Power in the United States. 2015.

(7) United States Department of Energy. Hydrogen strategy: Enabling a Low-Carbon Economy. https://www.energy.gov/sites/prod/files/2020/07/f76/USDOE_FE_Hydrogen_Strategy_July2020.pdf (accessed Mar 27, 2023).

(8) Hydrogen production: Natural gas reforming. https://www.energy.gov/eere/fuelcells/hydrogen-production-natural-gas-reforming (accessed Mar 27, 2023).

(9) Brandl, P.; Bui, M.; Hallett, J. P.; Mac Dowell, N. Beyond 90% Capture: Possible, but at What Cost? *International Journal of Greenhouse Gas Control* 2021, *105*, 103239.

(10) Fuel prices. https://afdc.energy.gov/fuels/prices.html (accessed Mar 27, 2023).

(11) Wainwright, M. The Mystery of the Plate: Fleming's Discovery and Contribution to the Early Development of Penicillin. *Journal of Medical Biography* 1993, *1* (1), 59–65.

(12) Markel, D. H. The real story behind penicillin. https://www.pbs.org/newshour/health/the-real-story-behind-the-worlds-first-antibiotic (accessed Mar 27, 2023).

(13) Zhang, H.; Sun, Z.; Hu, Y. H. Steam Reforming of Methane: Current States of Catalyst Design and Process Upgrading. *Renewable and Sustainable Energy Reviews* 2021, *149*, 111330.

(14) Stephenson, M.; Stickland, L. H. Hydrogenase: A Bacterial Enzyme Activating Molecular Hydrogen. *Biochemical Journal* 1931, *25* (1), 205–214.

(15) Guiral, M.; Prunetti, L.; Aussignargues, C.; Ciaccafava, A.; Infossi, P.; Ilbert, M.; Lojou, E.; Giudici-Orticoni, M.-T. The Hyperthermophilic Bacterium *Aquifex aeolicus*. *Advances in Microbial Physiology* 2012, 125–194.

(16) Näther Daniela J.; Rachel, R.; Wanner, G.; Wirth, R. Flagella of Pyrococcus Furiosus: Multifunctional Organelles, Made for Swimming, Adhesion to Various Surfaces, and Cell-Cell Contacts. *Journal of Bacteriology* 2006, *188* (19), 6915–6923.

(17) Greening, C.; Biswas, A.; Carere, C. R.; Jackson, C. J.; Taylor, M. C.; Stott, M. B.; Cook, G. M.; Morales, S. E. Genomic and Metagenomic Surveys of Hydrogenase Distribution Indicate H2 Is a Widely Utilised Energy Source for Microbial Growth and Survival. *The ISME Journal* 2015, *10* (3), 761–777.

(18) Vansuch, G. The Bioinorganic Energy Conversion Puzzle: Pieces from a [NiFe]-Hydrogenase Ligand Scaffold. Ph.D. Dissertation, Emory University: Atlanta, GA, 2021.

(19) Vignais, P.; Meyer, J.; Billoud, B. Classification and Phylogeny of Hydrogenases. *FEMS Microbiology Reviews* 2001, *25* (4), 455–501.

(20) Ahmed, M. E.; Dey, A. Recent Developments in Bioinspired Modelling of [NiFe]- and [FeFe]-Hydrogenases. *Current Opinion in Electrochemistry* 2019, *15*, 155–164.

(21) Brezinski, W. P.; Karayilan, M.; Clary, K. E.; Pavlopoulos, N. G.; Li, S.; Fu, L.; Matyjaszewski, K.; Evans, D. H.; Glass, R. S.; Lichtenberger, D. L.; Pyun, J. [FeFe]-Hydrogenase Mimetic Metallopolymers with Enhanced Catalytic Activity for Hydrogen Production in Water. *Angewandte Chemie International Edition* 2018, *57* (37), 11898–11902.

(22) Madden, C.; Vaughn, M. D.; Díez-Pérez, I.; Brown, K. A.; King, P. W.; Gust, D.; Moore, A. L.; Moore, T. A. Catalytic Turnover of [FeFe]-Hydrogenase Based on Single-Molecule Imaging. *Journal of the American Chemical Society* 2011, *134* (3), 1577–1582.

(23) Kubas, G. J. Fundamentals of $H_2$ Binding and Reactivity on Transition Metals Underlying Hydrogenase Function and $H_2$ Production and Storage. *Chemical Reviews* 2007, *107* (10), 4152–4205.

(24) Adams, M. W. W.; Mortenson, L. E.; Chen, J.-S. Hydrogenase. *Biochimica et Biophysica Acta (BBA) - Reviews on Bioenergetics* 1980, *594* (2-3), 105–176.

(25) Krasna, A. I.; Rittenberg, D. The Mechanism of Action of the Enzyme Hydrogenase. *Journal of the American Chemical Society* 1954, *76* (11), 3015–3020.

(26) Ma, K.; Adams, M. W. W. [18] Hydrogenases I and II from *Pyrococcus furiosus*. *Hyperthermophilic enzymes Part B* 2001, 208–216.

(27) Greene, B. L.; Wu, C.-H.; McTernan, P. M.; Adams, M. W.; Dyer, R. B. Proton-Coupled Electron Transfer Dynamics in the Catalytic Mechanism of a [NiFe]-Hydrogenase. *Journal of the American Chemical Society* 2015, *137* (13), 4558–4566.

(28) Greene, B. L.; Wu, C.-H.; Vansuch, G. E.; Adams, M. W.; Dyer, R. B. Proton Inventory and Dynamics in the Nia-S to Nia-C Transition of a [NiFe] Hydrogenase. *Biochemistry* 2016, *55* (12), 1813–1825.

(29) Ogata, H.; Nishikawa, K.; Lubitz, W. Hydrogens Detected by Subatomic Resolution Protein Crystallography in a [NiFe] Hydrogenase. *Nature* 2015, *520* (7548), 571–574.

(30) Wittkamp, F.; Senger, M.; Stripp, S. T.; Apfel, U.-P. [FeFe]-Hydrogenases: Recent Developments and Future Perspectives. *Chemical Communications* 2018, *54* (47), 5934–5942.

(31) Karayilan, M.; McCleary-Petersen, K. C.; Hamilton, M. O. B.; Fu, L.; Matyjaszewski, K.; Glass, R. S.; Lichtenberger, D. L.; Pyun, J. Synthesis of Metallopolymers via Atom Transfer Radical Polymerization from a [2Fe-2S] Metalloinitiator: Molecular Weight Effects on Electrocatalytic Hydrogen Production. *Macromolecular Rapid Communications* 2019, *41* (1), 1900424.

(32) Tai, H.; Nishikawa, K.; Higuchi, Y.; Mao, Z.; Hirota, S. Cysteine SH and Glutamate COOH Contributions to [NiFe] Hydrogenase Proton Transfer Revealed by Highly Sensitive FTIR Spectroscopy. *Angewandte Chemie International Edition* 2019, *58* (38), 13285–13290.

(33) Dementin, S.; Burlat, B.; De Lacey, A. L.; Pardo, A.; Adryanczyk-Perrier, G.; Guigliarelli, B.; Fernandez, V. M.; Rousset, M. A Glutamate Is the Essential Proton Transfer Gate during the Catalytic Cycle of the [NiFe] Hydrogenase. *Journal of Biological Chemistry* 2004, *279* (11), 10508–10513.

(34) VOLBEDA, A. High-Resolution Crystallographic Analysis of *Desulfovibrio fructosovorans* [NiFe] Hydrogenase. *International Journal of Hydrogen Energy* 2002, *27* (11-12), 1449–1461.

(35) Kwan, P.; McIntosh, C. L.; Jennings, D. P.; Hopkins, R. C.; Chandrayan, S. K.; Wu, C.-H.; Adams, M. W.; Jones, A. K. The [NiFe]-Hydrogenase of *Pyrococcus furiosus* Exhibits a New Type of Oxygen Tolerance. *Journal of the American Chemical Society* 2015, *137* (42), 13556–13565.

(36) Evans, R. M.; Ash, P. A.; Beaton, S. E.; Brooke, E. J.; Vincent, K. A.; Carr, S. B.; Armstrong, F. A. Mechanistic Exploitation of a Self-Repairing, Blocked Proton Transfer Pathway in an $O_2$-

Tolerant [NiFe]-Hydrogenase. *Journal of the American Chemical Society* 2018, *140* (32), 10208–10220.

(37) Burgdorf, T.; De Lacey, A. L.; Friedrich Bärbel. Functional Analysis by Site-Directed Mutagenesis of the NAD + -Reducing Hydrogenase from *Ralstonia Eutropha*. *Journal of Bacteriology* 2002, *184* (22), 6280–6288.

(38) Szőri-Dorogházi, E.; Maróti, G.; Szőri, M.; Nyilasi, A.; Rákhely, G.; Kovács, K. L. Analyses of the Large Subunit Histidine-Rich Motif Expose an Alternative Proton Transfer Pathway in [NiFe] Hydrogenases. *PLoS ONE* 2012, *7* (4).